

Linear impurity modes in an electrical lattice: Theory and experiment

M. I. Molina^{1,*}, L. Q. English,² Ming-Hua Chang,² and P. G. Kevrekidis^{3,4}

¹Departamento de Física, Facultad de Ciencias, Universidad de Chile, Santiago, Chile

²Department of Physics and Astronomy, Dickinson College, Carlisle, Pennsylvania 17013, USA

³Department of Mathematics and Statistics, University of Massachusetts, Amherst, Massachusetts 01003-4515, USA

⁴Mathematical Institute, University of Oxford, Oxford OX2 6GG, UK



(Received 1 October 2019; published 12 December 2019)

We examine theoretically and experimentally the localized electrical modes existing in a bi-inductive electrical lattice containing a bulk or a surface capacitive impurity. By means of the formalism of lattice Green's functions, we are able to obtain closed-form expressions for the frequencies of the impurity (bound-state) eigenmodes and for their associated spatial profiles. This affords us a systematic understanding of how these mode properties change as a function of the system parameters. We test these analytical results against experimental measurements, in both the bulk and surface cases, and find very good agreement. Last, we turn to a series of quench experiments, where either a parameter of the lattice or the lattice geometry itself is rapidly switched between two values or configurations. In all cases, we are able to naturally explain the results of such quench experiments from the larger analytical picture that emerges as a result of the detailed characterization of the impurity-mode solution branches.

DOI: [10.1103/PhysRevE.100.062114](https://doi.org/10.1103/PhysRevE.100.062114)

I. INTRODUCTION

In solid-state physics, it is a well established fact that lattices can feature localized modes in the presence of point defects, such as chemical impurities, vacancies, or interstitials, that break the shift translational invariance of the perfect lattice [1,2]. This type of disorder-induced localization can change the macroscopic properties of the crystal, its photon absorption spectrum (i.e., color) being a well-known example, but can also be responsible for a variety of interesting scattering phenomena [3]. Related applications abound in a diverse array of themes, ranging from defect modes in photonic crystals [4] as well as optical waveguide arrays [5–7] to superconductors [8] and from dielectric superlattices with embedded defect layers [9] to electron-phonon interactions [10] and granular crystals in materials science [11].

A related theme that is of particular interest concerns the existence of localized modes at the surface (i.e., at the ends) of linear chains due to the finite-size effect or, otherwise stated, the imposition of different kinds of boundary conditions. This type of exploration has also been a topic of consideration for over half a century, dating back to the early considerations of R. F. Wallis on the effects of free ends in one-dimensional [12] as well as surface modes in two- and three-dimensional lattices [13]. It is remarkable that the relevant considerations continue to inspire recent work, either on the theoretical role of different types of boundary conditions [14] or on modern applications including those of phononic crystals [15] that may also involve transversal-rotational modes [16].

In the present work, we take advantage of the well-established framework of electrical transmission lines [17,18] as a prototypical setting where the theory of linear impurity modes can be tested. On modeling the experimental setting of recent experiments such as in Refs. [19–21] at the linear level (i.e., in the absence of nonlinearity), we utilize the formulation of Green's functions [22–24] in order to identify both the eigenvalues or eigenfrequencies and eigenfunctions of the linear modes of the lattice, focusing naturally on the localized vibrations thereof. We provide analytical expressions for these and a systematic comparison with the corresponding experimental results. This is done not only for the linear lattice with a defect but also in the case of existence of a localized surface mode. Very good agreement is achieved between the two. Beyond that, there are some interesting observations and twists offered. In particular, it is found that in each range of frequencies (i.e., both above and below the linear band), only one mode can be identified theoretically and observed experimentally. Additionally, quench-type experiments are performed where we vary the parameter controlling the detuning from the homogeneous limit. In these we explore how the experimental lattice “jumps” from one value to the other and the lattice response accordingly transforms itself under such a quench. Finally, we also examine the voltage dynamics on the lattice during a switching transformation in its geometry from a line with an edge impurity into a ring with a bulk impurity.

Our presentation will be structured as follows. In Sec. II, we will present the physical setup and mathematical model. In Sec. III, we will provide details of the Green's function formalism for identifying the corresponding localized modes. In Sec. IV, we present our corresponding experimental results. Finally, in Sec. V, we summarize our conclusions and provide some directions for future study.

*mmolina@uchile.cl

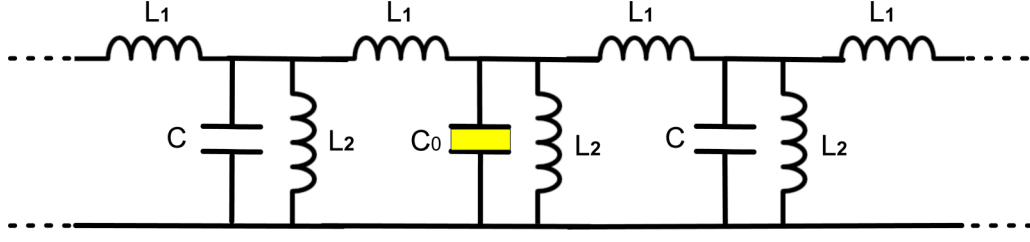


FIG. 1. Bi-inductive electrical lattice containing a single capacitive impurity (in line with Remoissenet *et al.* [17,18]).

II. THE MODEL

Our physical setup is that of Refs. [17,18] (see also Refs. [19–21] for some recent experimental studies in this system). In particular, we consider the bi-inductive electrical lattice shown in Fig. 1. It consists on N units composed of LC resonators $\{L_2, C_n\}$ coupled inductively by an inductor L_1 . If we call Q_n and V_n , respectively, the charge stored on the n th capacitor and the voltage drop across the inductor L_2 , then the use of the Kirchhoff laws leads to a system of coupled equations

$$\frac{d^2Q_n}{dt^2} = \frac{1}{L_1}(V_{n+1} + V_{n-1} - 2V_n) - \frac{1}{L_2}V_n. \quad (1)$$

The impurity at the center of our current considerations is assumed to be a capacitive one located at $n = 0$, with capacitance C_0 . The rest of the capacitances are taken as identical and equal to C . In other words, $C_n = C + (C_0 - C)\delta_{n,0}$.

By taking $Q_n = C_n V_n$ and $V_n(t) \sim \cos(\Omega t + \phi_n)$, we arrive at the stationary equations, i.e., the eigenvalue problem:

$$\begin{aligned} \Omega^2 U_n &= -\omega_1^2 (U_{n+1} + U_{n-1} - 2U_n) + \omega_2^2 U_n \\ &- (\Delta C/C) \Omega^2 \delta_{n,0} U_n, \end{aligned} \quad (2)$$

where $\Delta C = C_0 - C$ and $U_n = V_n/V_c$ is a dimensionless voltage, where V_c is a characteristic voltage. By means of simple manipulations, we can rearrange Eq. (2) as

$$z U_n = \gamma (U_{n+1} + U_{n-1}) + \epsilon \delta_{n,0} U_n \quad (3)$$

with

$$\begin{aligned} z &\equiv \Omega^2 - 2\omega_1^2 - \omega_2^2 \\ \gamma &\equiv -\omega_1^2 \\ \epsilon &\equiv -(\Delta C/C)\Omega^2, \end{aligned}$$

where $\omega_1^2 = 1/(L_1 C)$, and $\omega_2^2 = 1/(L_2 C)$.

Equation (3) describes formally a single impurity tight-binding model, whose Hamiltonian is given by

$$H = H_0 + H_d. \quad (4)$$

Using Dirac's notation, we can express H_0 and H_d in terms of Wannier functions $\{|n\rangle\}$ as

$$H_0 = \gamma \sum_n (|n+1\rangle\langle n| + |n\rangle\langle n+1|), \quad (5)$$

the (undisturbed) lattice Hamiltonian, and

$$H_d = \epsilon |0\rangle\langle 0|, \quad (6)$$

the *defect* (or impurity) Hamiltonian. The Hamiltonian H_0 describes the lattice without the impurity and, as is well

known, possesses plane-wave eigenvectors,

$$|n|k\rangle = (1/\sqrt{N}) \exp(ikn), \quad (7)$$

and eigenvalues,

$$z_k = 2\gamma \cos(k), \quad (8)$$

or, in terms of the electrical lattice parameters,

$$\Omega^2 = 4\omega_1^2 \sin^2(k/2) + \omega_2^2. \quad (9)$$

Thus, the system is able to support the propagation of electrical waves that form a band extending (in terms of Ω^2) from ω_2^2 to $\omega_2^2 + 4\omega_1^2$. Notice that in the infinite lattice limit this band would be a continuous spectrum, while in the finite lattice case, the boundary conditions select a specific set of wave numbers k (e.g., $k_m = m\pi/N$ with m integer running up to N for periodic boundary conditions), and thus only the corresponding frequencies are observed.

III. THE GREEN'S FUNCTION FORMALISM

Given a Hamiltonian H , the lattice Green's function is defined as [22–24]

$$G(z) = 1/(z - H). \quad (10)$$

In our case, $H = H_0 + H_d$. Treating H_d formally as a perturbation, we can express $G(z)$ as

$$G(z) = G^{(0)} + G^{(0)} H_d G^{(0)} + G^{(0)} H_d G^{(0)} H_d G^{(0)} + \dots, \quad (11)$$

where $G^{(0)} = 1/(z - H_0)$ is the unperturbed Green function. Inserting $H_d = \epsilon |0\rangle\langle 0|$, we have

$$\begin{aligned} G(z) &= G^{(0)} + \epsilon G^{(0)} |0\rangle\langle 0| G^{(0)} \\ &+ \epsilon^2 G^{(0)} |0\rangle\langle 0| G^{(0)} |0\rangle\langle 0| G^{(0)} + \dots \\ &= G^{(0)} + \epsilon G^{(0)} |0\rangle \left[\sum_{n=0}^{\infty} \epsilon^n G_{00}^{(0)n} \right] \langle 0| G^{(0)} \\ &= G^{(0)} + \frac{G^{(0)} |0\rangle \epsilon \langle 0| G^{(0)}}{1 - \epsilon G_{00}^{(0)}}. \end{aligned}$$

In this expression, we use the notation: $G_{00}^{(0)} = \langle 0|G^{(0)}|0\rangle$. It can thus be easily proven that the eigenenergies of the localized modes are given by the poles of G , while the probability amplitudes are given by the residues of G at those poles.

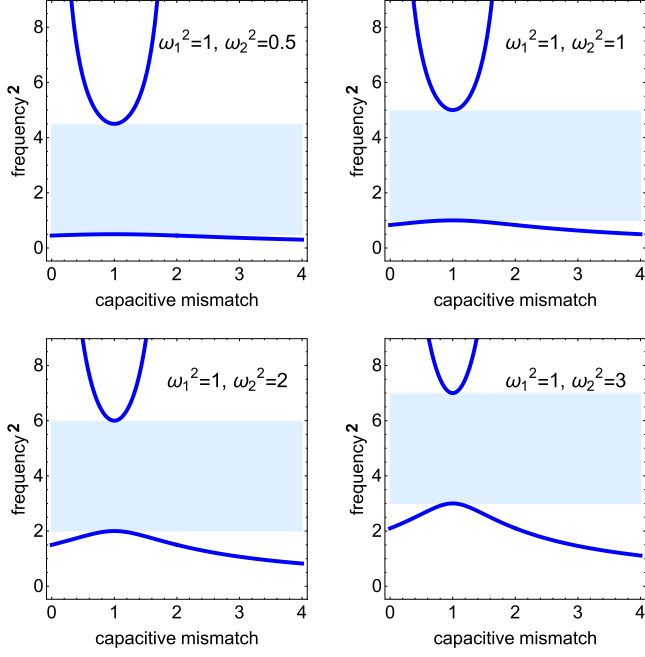


FIG. 2. Eigenfrequencies of the localized mode versus the capacitive mismatch for several ω_1, ω_2 values. Recall that for $\delta < 1$ only the higher frequencies (above the band) are physically relevant, while for $\delta > 1$ only the lower frequencies (below the band) are physically relevant (among the two branches shown). This will be an important observation to bear in mind also for the physical experiments that will follow.

A. Electrical impurity in the bulk

Let us consider a capacitive defect that is located far from the boundaries of the system. In that case we have from Ref. [22] that:

$$G_{00}^{(0)}(z) = \frac{\text{sgn}(z)}{\sqrt{z^2 - (2\gamma)^2}}. \quad (12)$$

After solving the energy equation $1/\epsilon = G_{00}^{(0)}(z_b)$, one obtains

$$z_b = \pm\sqrt{\epsilon^2 + (2\gamma)^2}. \quad (13)$$

In terms of our electrical parameters, this leads to

$$\Omega^2 = \frac{-(2\omega_1^2 + \omega_2^2) \pm \sqrt{4\omega_1^4 + (\delta - 1)^2\omega_2^2(4\omega_1^2 + \omega_2^2)}}{\delta(\delta - 2)}, \quad (14)$$

where $\delta = C_0/C$ is the capacitive mismatch. However, it should be kept in mind that only one of the branches corresponds to each case: the $(-)$ one in Eq. (14) for $C_0 < C$ or $\delta < 1$ and the $(+)$ one in Eq. (14) for $C_0 > C$ or $\delta > 1$. Figure 2 shows the theoretically predicted energy branches as a function of the capacitive mismatch δ for several different resonant frequencies ω_1^2, ω_2^2 . All eigenfrequencies Ω^2 lie outside of the band. In the absence of the defect, i.e., for $\delta = 1$, the solutions touch the band right at the edges of the band. These edge modes are the ones that detach from the band due to the presence of the defect.

For the bound-state profile $|b\rangle$, we start from $|b\rangle = \sum_n b_n |n\rangle$, where b_n is the mode amplitude profile and is given

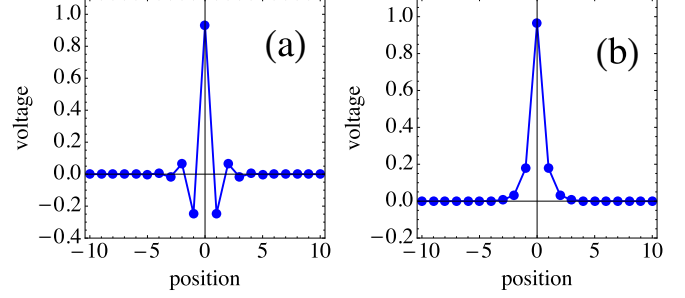


FIG. 3. Spatial profiles of the localized electrical bulk modes for $\omega_1 = 1 = \omega_2$; (a) $\delta = 0.5$ (upper branch) and (b) $\delta = 3$ (lower branch).

by the residue of $G(z)$ at $z = z_b$,

$$b_n = \frac{G_{n0}(z_b)}{\sqrt{-G'_{00}(z_b)}}, \quad (15)$$

where

$$G_{n0}(z) = \frac{\text{sgn}(z)}{\sqrt{z^2 - (2\gamma)^2}} \left\{ -\left(\frac{z}{2|\gamma|}\right) + \text{sgn}(z) \sqrt{\left(\frac{z}{2\gamma}\right)^2 - 1} \right\}^{|n|}. \quad (16)$$

We obtain:

$$b_n = \text{sgn}(z_b) \frac{[z_b^2 - (2\gamma)^2]^{1/4}}{|z_b|^{1/2}} \left\{ -\left(\frac{z_b}{2|\gamma|}\right) + \text{sgn}(z_b) \sqrt{\left(\frac{z_b}{2\gamma}\right)^2 - 1} \right\}^{|n|}, \quad (17)$$

where $z_b = \Omega^2 - 2\omega_1^2 - \omega_2^2$, $|\gamma| = \omega_1^2$, and Ω^2 is given by Eq. (14). Recall that $z_b > 0$ for $\delta < 1$, while $z_b < 0$ for $\delta > 1$. Figure 3 shows the spatial profile of the bound state for different electrical parameters, namely for $\delta < 1$ and $\delta > 1$. The mode width decreases with either an increase in capacitive mismatch (associated with δ) or an increase in frequency mismatch $|\omega_1^2 - \omega_2^2|$.

B. Electrical impurity at the boundary

Now we consider the case where the defect is placed at the very surface of a semi-infinite electrical array (Fig. 4). Computation of the proper Green's function for this case requires realizing that, even though the main formalism is still the same as in Sec. III A, the unperturbed Green's function $G_{mn}^{(0)}$ needs to be computed by the method of mirror images: since there is no lattice to the left of $n = 0$, $G_{mn}^{(0)}$ must vanish identically at $n = -1$. This means $G_{mn}^{(0)}(z) = G_{mn}^{\infty}(z) - G_{m,-n-2}^{\infty}(z)$, where $G_{mn}^{\infty}(z)$ is the unperturbed Green's function of the bulk case: $G_{mn}^{\infty}(z) = \text{sgn}(z)(1/\sqrt{z^2 - 1})[z - \text{sgn}(z)\sqrt{z^2 - 1}]^{|n-m|}$. The procedure for computing the frequency of the surface bound state and its profile is exactly the same as in Sec. III A, and it is detailed in the Appendix.

Figure 5 shows the eigenfrequency Ω^2 of the bound state as a function of the capacitive mismatch δ . An interesting feature of Ω^2 in this case (with the boundary) concerns the forbidden bands inside which there are no bound states. In terms of

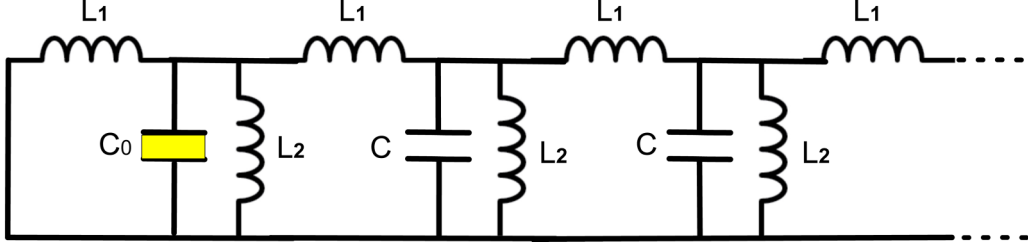


FIG. 4. Bi-inductive electrical lattice containing a single surface capacitive impurity (in line with Remoissenet *et al.* [17,18]).

frequencies, there exists the well-known frequency band that extends from ω_2^2 to $\omega_2^2 + 4\omega_1^2$. In terms of the parameter δ , there exists an interval in capacitive mismatch that extends from $\delta = 1$ to

$$\delta_1 = \frac{(2\omega_1^2 + \omega_2^2)^2}{4\omega_1^2\omega_2^2 + \omega_2^4}, \quad (18)$$

inside which the mode is complex. The most important intervals, however, are the ones originating from the condition that the capacitance mismatch $|\delta - 1|$ be sufficiently large to produce a bound state. These are given by $\delta < \delta_2$ and $\delta > \delta_3$, where

$$\delta_2 = \frac{3\omega_1^2 + \omega_2^2}{4\omega_1^2 + \omega_2^2} < 1, \quad \delta_3 = 1 + \left(\frac{\omega_1}{\omega_2}\right)^2 > 1. \quad (19)$$

The origin of this condition lies in the fact that the real part of the surface Green's function, $G_{00}^{(0)}(z)$ for z outside the band, is bounded from above and below, unlike the case of the bulk Green's function. Of the different critical δ values only δ_2 and δ_3 are relevant since $\delta_2 < 1$ and $\delta_3 > \delta_1$. It can be also proven that at $\delta = \delta_{2,3}$ the energy curves touch the linear band. These features can be appreciated in Fig. 5.

Figure 6 shows once again some spatial mode profiles. We now turn to the experimental realization of the above localized modes.

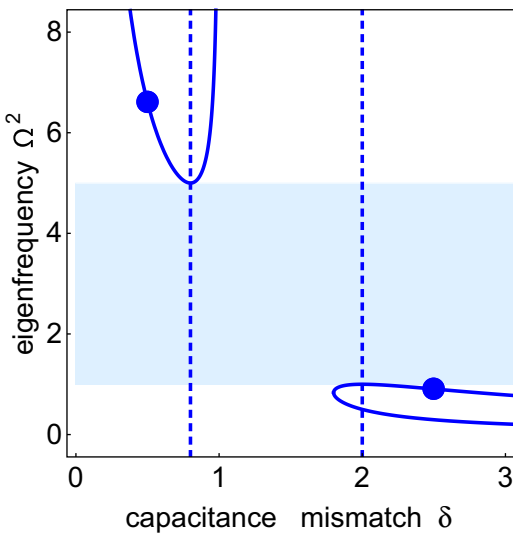


FIG. 5. Eigenfrequencies Ω^2 of the electrical surface mode, in terms of the capacitance mismatch δ for $\omega_1^2 = 1 = \omega_2^2$. The dashed lines mark the position of the critical δ values $\delta_2 = 0.8$ and $\delta_3 = 2$.

IV. THE EXPERIMENT

We have built the bi-inductance lattice shown in Fig. 1 made up of discrete electrical elements of inductors and capacitors. The inductors were ferrite (radial-lead) inductors of $470 \mu\text{H}$ inductance and about 1Ω resistance (equivalent series resistance, ESR). We used these inductors both as the L_1 and L_2 elements in a lattice with $\omega_2^2 \approx \omega_1^2$. The inductance values were all within 1% of one another. One set of measurements was also done on a lattice with $\omega_2^2 \approx 2\omega_1^2$, and there we also incorporated $975 \mu\text{H}$ inductors with an ESR of 2Ω . The fixed capacitors, C , were all of 1 nF capacitance to within 2% of one another. In addition, in order to excite any mode we incorporated a driving signal using an arbitrary function generator (Agilent 33220A) whose signal was injected into the electrical lattice via $10\text{-k}\Omega$ resistors. The voltages at each lattice node were monitored using multichannel data acquisition boards (National Instruments PXI-6133).

The impurity was introduced via the replacement at one lattice site of the 1-nF capacitor with a varactor diode (NTE-618) whose capacitance can be continuously varied by applying a bias voltage. The capacitance-voltage relationship for the varactor diode was carefully mapped out by separately measuring the resonance curve of an RLC circuit that incorporated this diode in parallel with a known inductor. When introducing such a bias voltage across the varactor diode, care must be taken, however, to ensure that none of the inductors in the lattice experiences a dc potential drop across them. This was achieved by using a large ($2\text{-}\mu\text{F}$) block capacitor in series with the varactor diode. In essence, then, we can continuously vary the δ parameter with a dc power supply that controls the bias voltage across the varactor diode. This yields a capacitance range for C_0 from about 900 pF to about 150 pF . Given our choice of $C = 1 \text{ nF}$, in order to attain the $\delta > 1$ regime, we

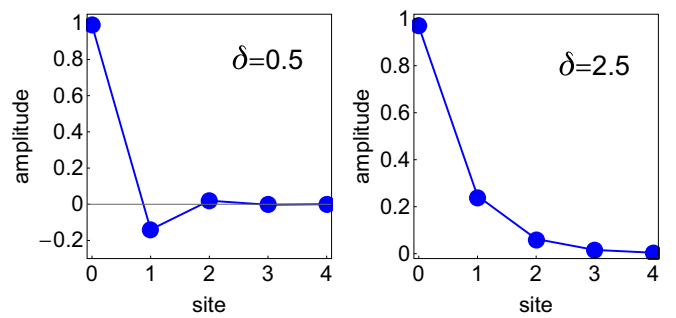


FIG. 6. Spatial profiles of the localized surface modes marked in Fig. 5 for $\delta = 0.5$ and $\delta = 2.5$.

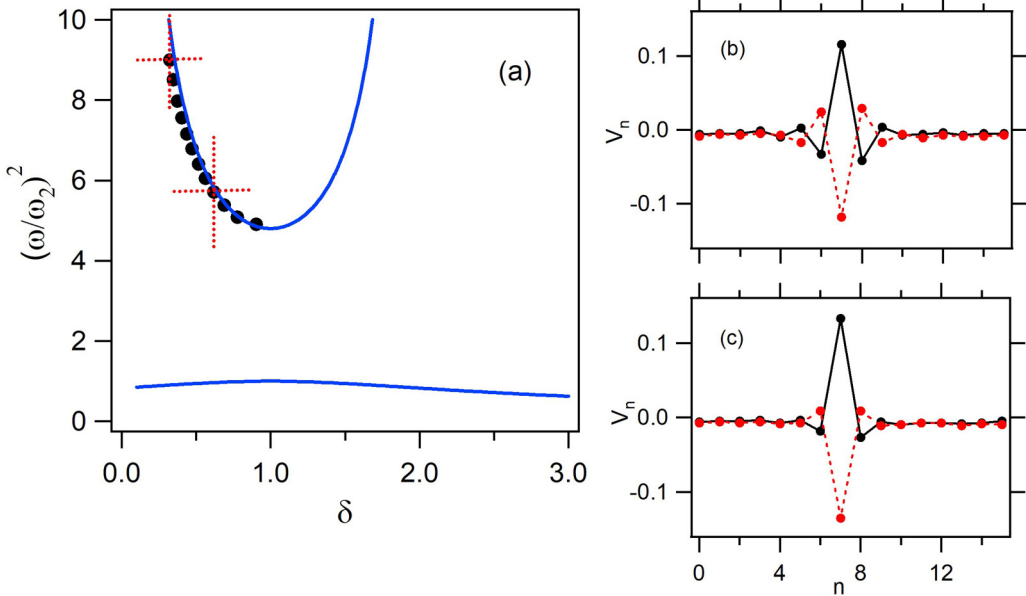


FIG. 7. (a) The experimental frequencies of the upper-branch impurity modes as a function of capacitance-mismatch parameter δ . The data fit the theoretical prediction quite well. Panels (b) and (c) depict measured mode profiles at $\delta = 0.62$ and $\delta = 0.32$, respectively. The times at which the center node is most positive and most negative are shown, respectively, by solid and dashed lines.

can place this varactor diode in parallel with a fixed 1- or 2-nF capacitor.

A. Impurity in the lattice bulk

To compare the experimental observations to the theoretical predictions in the previous section, Fig. 7(a) depicts the square of the normalized frequencies, $(\omega/\omega_2)^2$, as a function of the capacitance-mismatch parameter, δ , which measures the strength of the impurity for the upper-branch localized modes. We see that the experimental data points (black circles) match the theoretical curve very well for the parameter values of $\omega_2^2 = 1$ and $\omega_1^2 = 0.95$. Importantly, as we highlighted in the theoretical section only one of the two solutions with frequencies above the band is selected in line with the theoretical prediction. To excite these impurity modes, we can use a sinusoidal waveform that is swept through a range of frequencies while simultaneously recording the impurity mode response. In this way a spectrum is generated, and the mode frequency is obtained from the peak's center frequency within that spectrum. The driving waveform can be applied uniformly at each site of the lattice or alternatively only at the impurity site. Both driving methods yield the same frequency information, although the exact mode profile does depend slightly on the driving method. Here we show results corresponding to local driving.

From the inductor values themselves, i.e., $L_1 = L_2 = 470 \mu\text{H}$, we would expect $\omega_1^2 = 1$. The fact that this value is slightly lower in the experimental system, however, is confirmed independently by separately measuring the zone-boundary (ZB) mode frequency. Here a spatially staggered driver is employed to probe the resonance curve associated with the ZB mode, and its center frequency is recorded at around 502 kHz. Given that the zone-center mode is

at $\omega_2/(2\pi) = 228 \text{ kHz}$, we would expect the ZB to be at approximately 510 kHz. The fact that it is found at somewhat lower frequency indicates that the effective ω_1 is also lower by a small amount.

Figures 7(b) and 7(c) show the measured spatial profiles of two impurity modes, corresponding to $\delta = 0.62$ and $\delta = 0.32$, respectively. The node voltages measured at two particular times are shown at which the voltage at the center node

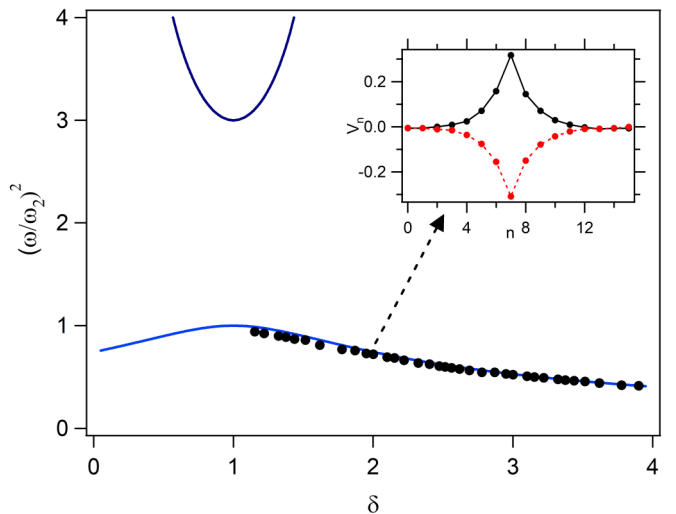


FIG. 8. The experimental frequencies of the lower-branch impurity modes as a function of the mismatch parameter δ . Again, the data fit the theoretical prediction quite well, with some slight deviation near $\delta = 1$. As explained in the previous section only the portion of the branch with $\delta > 1$ is physically relevant and hence experimentally observed. The inset depicts the measured mode profile at $\delta = 2.0$.

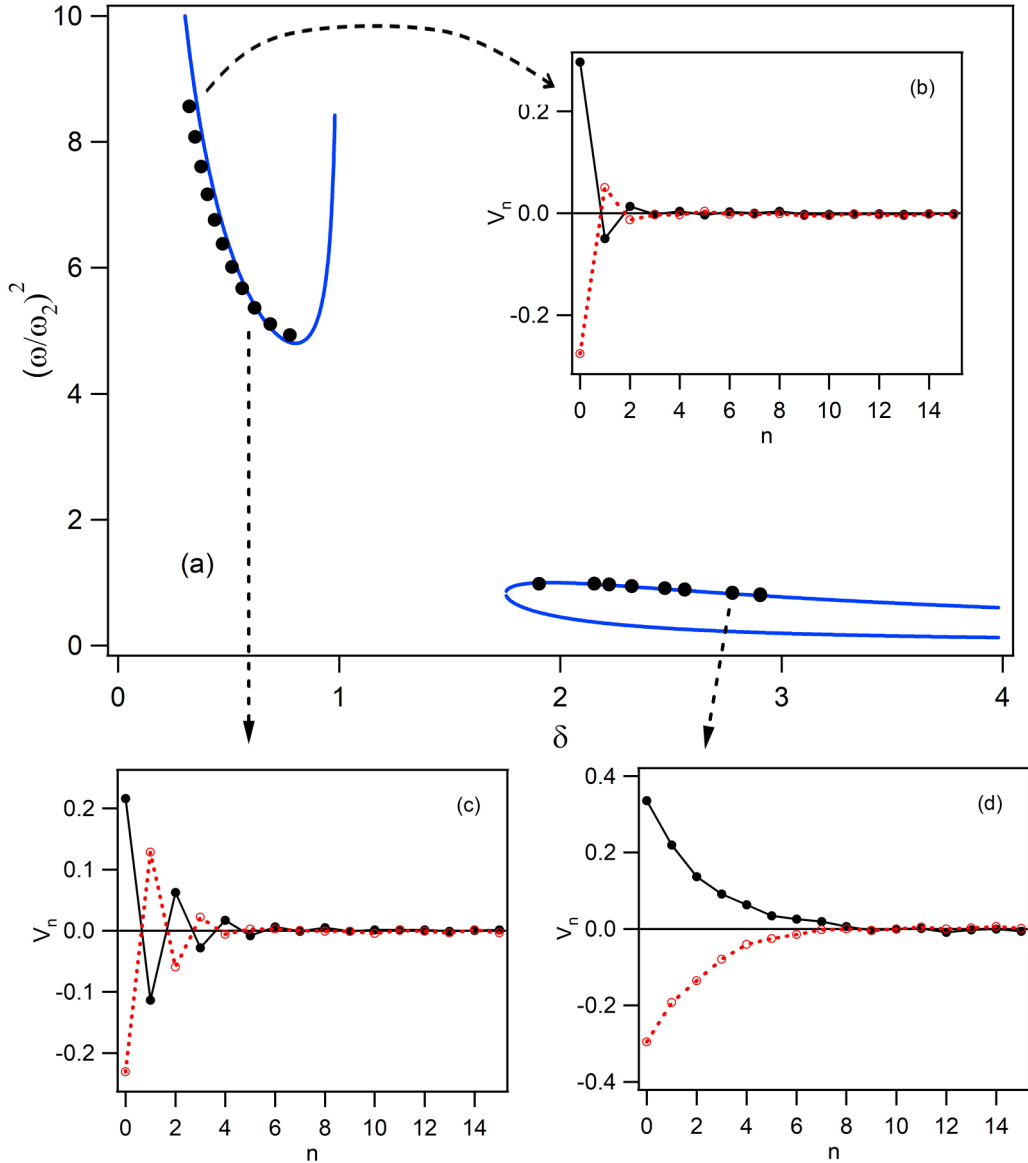


FIG. 9. (a) The experimental frequencies of the surface impurity modes as a function of the capacitance-mismatch parameter δ ; both upper-branch and lower-branch solutions are shown. The theoretical prediction is depicted by the solid curves with only the left branch being relevant for $\delta < \delta_2$ and the top branch for $\delta > \delta_3$. Panels (b)–(d) show the measured profiles of three particular surface modes, located at $\delta = 0.32$, $\delta = 0.62$, and $\delta = 2.78$, respectively.

($n = 7$) is most positive and most negative, respectively. As also seen in the theoretical waveforms, the farther δ departs from 1, and thus the higher the frequency, the more localized the impurity mode is in space.

We now turn to the lower-branch modes in this lattice. From the theoretical picture of Fig. 2, we discern that when ω_2 is raised relative to ω_1 , the branch descends away from the bottom of the plane-wave spectrum more rapidly. (The same is also true in the case when ω_1 is lowered relative to ω_2 .) For this reason, we decided to decrease the coupling strength—and thus ω_1 —while leaving ω_2 unchanged when observing the lower branch. This was accomplished by using coupling inductors of $L_1 = 975 \mu\text{H}$.

Figure 8 depicts the experimental results on the lower branch. The lines represent the theoretical curves given in Eq. (14) for $\omega_2^2 = 1$ and $\omega_1^2 = 0.475$. We again see good

agreement between theory and experiment, although some deviation is observed for δ values close to 1, where the localized mode becomes quite broad (and where perhaps a larger lattice would thus be needed). Recall that per our theoretical analysis, only the portion of the branch with $\delta > 1$ is physical (and thus experimentally traceable). The inset panel shows the impurity mode profile. We see that, contrary to the upper-branch modes where neighboring sites oscillate out of phase, for these lower-branch impurity modes the nodes all oscillate in-phase. Thus, the impurity modes in both instances share the basic symmetry with that plane-wave mode into which they merge as $\delta \rightarrow 1$.

B. Impurity at the boundary

It is straightforward to transform the electrical lattice used so far into a lattice where the impurity is at its boundary.

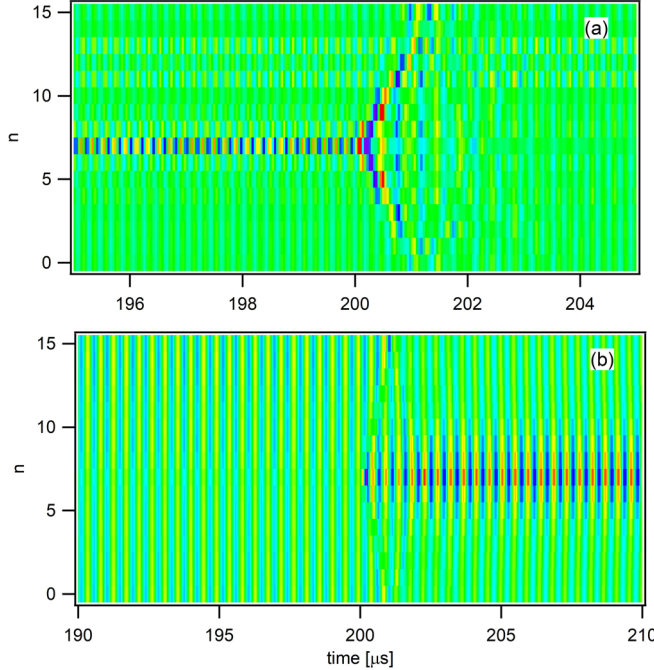


FIG. 10. Space n -time t contour plot evolution of quench experiments for the voltage $V_n(t)$: (a) From $\delta = 0.57$, we quench to $\delta = 1.43$ in the case of the upper branch; (b) the same is done in the case of the lower branch. The two panels clearly illustrate in line also with the theory that the upper frequency branch only exists for $\delta < 1$, while the lower frequency branch only for $\delta > 1$.

We simply disconnect the far end of the coupling inductor at $n = 7$ and instead ground it. We also return to the case $L_1 = 470 \mu\text{H}$, such that $\omega_2^2 = 1$, $\omega_1^2 = 0.95$.

Confirming the theoretical prediction, no surface modes are found within the interval of $0.80 < \delta < 1.95$. For $\delta < \delta_2 = 0.80$, we observe upper-branch solutions and for $\delta > \delta_3 = 1.95$ lower-branch solutions. Their frequencies nicely match the theoretical prediction, as seen in Fig. 9(a). Figures 9(b) and 9(c) show the spatial profiles of the upper-branch modes measured at the two δ values of 0.32 and 0.62, respectively. As expected, we clearly observe the mode widening in space as δ approaches 1. Figure 9(d) depicts the lower-branch mode at $\delta = 2.78$. The width of the mode is somewhat larger than what is obtained in the analysis; one possible reason might be that experimentally some part of the uniform mode may still be excited.

C. Quench experiments

In order to examine the impact of quenches and the response of the system between the two fundamentally different regimes examined ($\delta < 1$ and $\delta > 1$ in the bulk and correspondingly also in the case of the surface), we devise the following quenching experiment. We use a single pole double throw analog switch, the chip ADG436, to rapidly switch between two capacitor values for C_0 : 0.57 and 1.43 nF. These two values were chosen because they are symmetrically situated relative to 1 nF. Again, the driving of the lattice can be either local (at the impurity) or the spatially homogenous

(shown in the following figures). For the upper-branch case in Fig. 10(a), the driving frequency corresponded to $\Omega^2 = 5.52$ (equivalent to 536 kHz). We see that at this frequency and for $C_0 = 0.57$ nF (corresponding to a δ of 0.57), the upper-branch impurity mode can be stably excited. When we abruptly switch to $\delta = 1.43$ at time $t = 200 \mu\text{s}$; however, the mode disintegrates and does not reconstitute itself. That is, there is no corresponding physical branch on the other side at $\delta = 1.43$.

A similar phenomenon can be discerned in Fig. 10(b) for the lower branch, where we chose a frequency of 219 kHz (or $\Omega^2 = 0.92$). Here no mode exists at $\delta = 0.57$, but on abruptly switching to $\delta = 1.43$, the lower-branch impurity mode emerges. We should mention that if we start with the larger value of δ and then switch to the lower one, no impurity mode is generated in that case either.

Another appealing switching experiment that can be performed in the present setting involves transforming the impurity mode from a surface one to a bulk one by using the analog switch to temporarily impose a boundary in the lattice that is otherwise ringlike. The switch connects the far end of the L_1 inductor at $n = 7$ first to ground and then abruptly to the L_1 inductor at $n = 8$. Here we chose a δ of 0.47 and excited the lattice with a spatially homogenous driver at various upper-branch frequencies. This is illustrated in Fig. 11(a), where the frequency corresponds to $\Omega^2 = 6.34$. The switch from boundary lattice bearing a surface to a ring lattice (i.e., a bulk one with periodic boundary conditions) occurs at 200 μs . We see that the initial surface mode naturally transforms itself into the bulk mode after the switch. Figures 11(b) and 11(c) decrease the driver frequency consecutively to $\Omega^2 = 5.86$ and 5.65, respectively. It is clear that the bulk mode is weakened in Fig. 11(b) and then disappears altogether in Fig. 11(c), while the surface mode is still generated at these frequencies.

This last result makes sense upon close comparison of Figs. 7(a) and 9(a), which (for convenience) is shown in Fig. 11(d). When superimposing the solution branches in the two cases, we see that the upper-branch surface modes have lower frequency compared to the bulk modes for all allowed δ values of the former (i.e., for $\delta < \delta_2$). Since the experimental system features dissipation and thus potential relaxation to the modes, those modes have some width in frequency and therefore can overlap, such that at a given driving frequency both can be excited. However, if the driving frequency is repeatedly lowered, then we first lose the bulk mode and only later the surface mode.

V. CONCLUSIONS AND FUTURE CHALLENGES

We have studied both theoretically and experimentally an electrical transmission-line lattice possessing a capacitive impurity point-defect located either at the bulk or at the boundary of the circuit. By using the formalism of lattice Green's functions, we were able to predict the existence of localized modes for which the voltage decreases in space as we move away from the defect position. We obtained in closed form the bound-state frequency of the impurity state, as well as the bound-state profile as a function of the parameters of the electrical circuit. Very good agreement

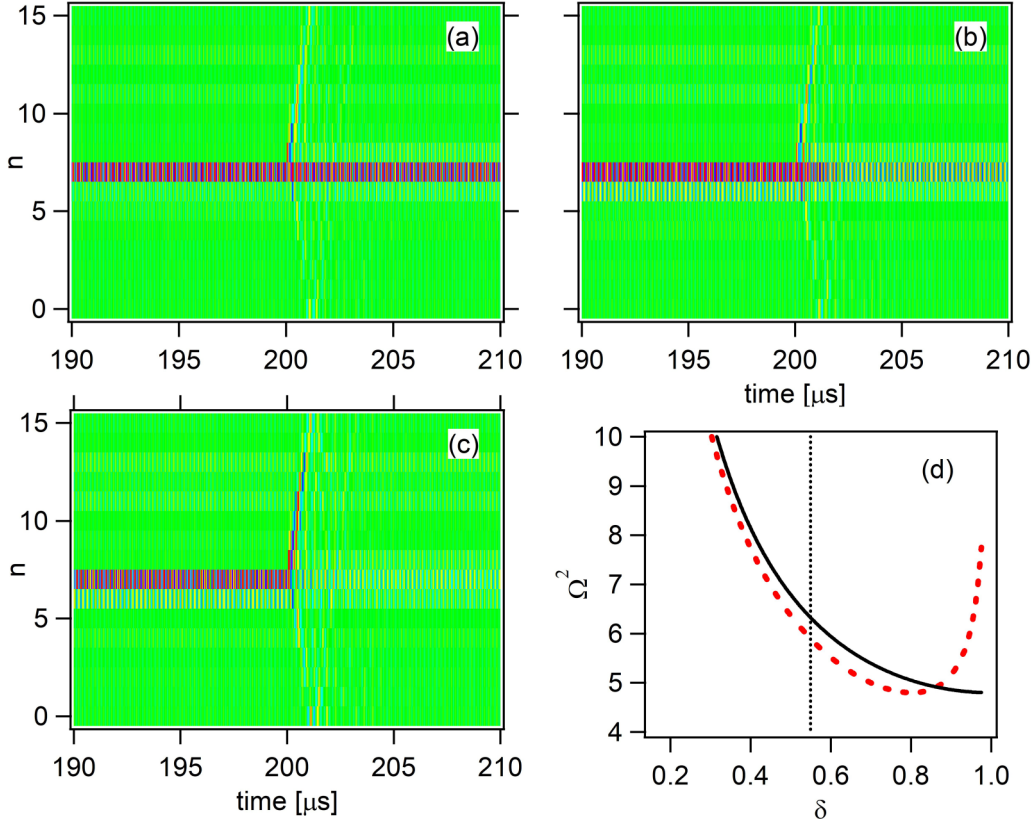


FIG. 11. Switching between a surface mode and a bulk mode by closing a switch to complete the ring at $t = 200 \mu\text{s}$. The driver frequency corresponds to Ω^2 of (a) 6.34, (b) 5.86, and (c) 5.65. While the surface impurity mode can be generated at all three frequencies, we see the bulk impurity mode unable to sustain itself in (c). This makes sense when comparing the frequencies of the solution branches in (d), where the dotted vertical line is the δ chosen in these experiments, and the solid and dashed lines are the upper-branch bulk and surface modes, respectively.

was observed between the theoretical predictions and the corresponding experimental results both for the bulk and also for the surface impurity modes. Additionally, quench-type experiments were performed by rapidly switching a lattice parameter and observing how the voltage profile adapts itself to such a modification. Also an interesting scenario of a switch from a bulk lattice to a surface one was explored and the spontaneous transformation of the bulk modes to surface ones was elucidated. Such experiments were found to be in accord with the analytical picture characterized by its relevant solution branches.

Naturally, this study and the systematic benchmarking of the linear lattice properties paves the way toward further explorations. At the linear level, the theory of Green's functions also permits an analytical characterization of the transmission problem from an impurity as a function of the wave number of the incoming wave, as well as of the impurity (and lattice) parameters. This is a technically more challenging problem as it arguably requires larger lattices than the ones considered herein, yet is, in principle, experimentally tractable. On the other hand, numerous studies have focused on nonlinear impurities in a linear lattice [10,25,26] as the first among the many different possible scenarios involving nonlinearity in the present setting. This is a natural next step for our studies and will be considered in future publications.

ACKNOWLEDGMENTS

M.I.M. acknowledges support from Fondo Nacional de Desarrollo Científico y Tecnológico (Fondecyt) Grant No. 1160177. P.G.K. gratefully acknowledges support from NSF-DMS-1809074, the hospitality of the Mathematics Institute of the University of Oxford, and the support of the Leverhulme Trust.

APPENDIX: SURFACE MODES

The bound-state energies are given by the poles of $G_{n,m}$, that is, $G_{0,0}^{(0)}(z) = 1/\epsilon$, where $G_{n,m}^{(0)} = G_{n,m}^\infty - G_{n,-m-2}^\infty$, $\epsilon = (1 - \delta)\Omega^2/2\omega_1^2$, and $z = \Omega^2 - 2\omega_1^2 - \omega_2^2$.

We obtain the eigenfrequencies as a function of the capacitance mismatch δ , as the residues of $G_{n,m}$ at the poles:

$$\Omega_\pm^2 = \frac{(2\omega_1^2 + \omega_2^2) \pm \sqrt{\frac{-4\omega_1^4}{\delta-1} + 4\omega_1^2\omega_2^2 + \omega_2^4}}{2\delta}. \quad (\text{A1})$$

The bound-state amplitudes are formally given by the residues of the surface Green function $G_{nm}(z)$, that is,

$$b_n^\pm = \frac{G_{n,0}^{(0)}[z(\delta)]}{\sqrt{-G_{n0}^{(0)\prime}[z(\delta)]}}, \quad (\text{A2})$$

where

$$G_{n,0}^{(0)}(z) = \frac{\text{sgn}(z)}{\sqrt{z^2 - 1}} \{ [z - \text{sgn}(z)\sqrt{z^2 - 1}]^{|n|} \} \quad (\text{A3})$$

$$- (z - \text{sgn}(z)\sqrt{z^2 - 1})^{|n+2|} \quad (\text{A4})$$

and

$$G_{n,0}^{(0)'}(z) = -\frac{2 \text{sgn}(z)}{\sqrt{z^2 - 1}} [z - \text{sgn}(z)\sqrt{z^2 - 1}]. \quad (\text{A5})$$

[1] A. A. Maradudin, E. W. Montroll, and G. H. Weiss, *Theory of Lattice Dynamics in the Harmonic Approximation* (Academic Press, New York, 1963).

[2] I. M. Lifschitz, *Nuovo Cimento, Suppl.* **3**, 716 (1956); I. M. Lifschitz and A. M. Kosevich, *Rep. Progr. Phys.* **29**, 217 (1966).

[3] A. A. Maradudin, *Sol. Stat. Phys.* **18**, 273 (1966).

[4] S. Y. Jin, E. Chow, V. Hietala, P. R. Villeneuve, and J. D. Joannopoulos, *Science* **282**, 274 (1998); M. G. Khazhinsky and A. R. McGurn, *Phys. Lett. A* **237**, 175 (1998).

[5] U. Peschel, R. Morandotti, J. S. Aitchison, H. S. Eisenberg, and Y. Silberberg, *Appl. Phys. Lett.* **75**, 1348 (1999).

[6] R. Morandotti, H. S. Eisenberg, D. Mandelik, Y. Silberberg, D. Modotto, M. Sorel, C. R. Stanley, and J. S. Aitchison, *Opt. Lett.* **28**, 834 (2003).

[7] E. Smirnov, C. E. Rüter, M. Stepić, V. Shandarov, and D. Kip, *Opt. Express* **14**, 11248 (2006).

[8] A. F. Andreev, *JETP Lett.* **46**, 584 (1987); A. V. Balatsky, *Nature* **403**, 717 (2000).

[9] E. Lidorikis, K. Busch, Q. Li, C. T. Chan, and C. M. Soukoulis, *Phys. Rev. B* **56**, 15090 (1997).

[10] M. I. Molina and G. P. Tsironis, *Phys. Rev. B* **47**, 15330 (1993); G. P. Tsironis, M. I. Molina, and D. Hennig, *Phys. Rev. E* **50**, 2365 (1994).

[11] G. Theocharis, M. Kavousanakis, P. G. Kevrekidis, Chiara Daraio, Mason A. Porter, and I. G. Kevrekidis, *Phys. Rev. E* **80**, 066601 (2009).

[12] R. F. Wallis, *Phys. Rev.* **105**, 540 (1957).

[13] R. F. Wallis, *Phys. Rev.* **116**, 302 (1959).

[14] Q. Luo, *Eur. J. Phys.* **37**, 065501 (2016).

[15] E. Kim and J. Yang, *J. Mech. Phys. Sol.* **71**, 33 (2014).

[16] H. Pichard, A. Duclos, J.-P. Groby, and V. Tournat, and V. E. Gusev, *Phys. Rev. E* **89**, 013201 (2014).

[17] M. Remoissenet, Linear waves in electrical transmission lines, in *Waves Called Solitons* (Springer-Verlag, Berlin, 1999).

[18] P. Marquie, J. M. Bilbault, and M. Remoissenet, *Phys. Rev. E* **51**, 6127 (1995).

[19] L. Q. English, R. B. Thakur, and R. Stearrett, *Phys. Rev. E* **77**, 066601 (2008).

[20] L. Q. English, F. Palmero, J. F. Stormes, J. Cuevas, R. Carretero-Gonzalez, and P. G. Kevrekidis, in Proceedings of the International Symposium on Nonlinear Theory and Applications, Santa Fe, Vol. 2 (2013), pp 334–337.

[21] X.-L. Chen, S. Abdoulkary, P. G. Kevrekidis, and L. Q. English, *Phys. Rev. E* **98**, 052201 (2018).

[22] E. Economou, *Green's Functions in Quantum Physics* (Springer-Verlag, Berlin, 1983).

[23] G. Barton, *Elements of Green's Functions and Propagation: Potentials, Diffusion, and Waves* (Oxford University Press, Oxford, 1989).

[24] D. G. Duffy, *Green's Functions with Applications* (Chapman & Hall/CRC, Boca Raton, FL, 2001).

[25] M. I. Molina and H. Bahlouli, *Phys. Lett. A* **294**, 87 (2002).

[26] H. Yue, M. I. Molina, P. G. Kevrekidis, and N. I. Karachalios, *J. Math. Phys.* **55**, 102703 (2014).